

## MULTIWAVELENGTH OBSERVATIONS OF SMALL-SCALE RECONNECTION EVENTS TRIGGERED BY MAGNETIC FLUX EMERGENCE IN THE SOLAR ATMOSPHERE

S. L. GUGLIELMINO<sup>1</sup>, L. R. BELLOT RUBIO<sup>2</sup>, F. ZUCCARELLO<sup>1</sup>, G. AULANIER<sup>3</sup>, S. VARGAS DOMÍNGUEZ<sup>4</sup> AND S. KAMIO<sup>5</sup>  
*Draft version September 1, 2018*

### ABSTRACT

The interaction between emerging magnetic flux and the pre-existing ambient field has become a “hot” topic for both numerical simulations and high-resolution observations of the solar atmosphere. The appearance of brightenings and surges during episodes of flux emergence is believed to be a signature of magnetic reconnection processes. We present an analysis of a small-scale flux emergence event in NOAA 10971, observed simultaneously with the Swedish 1-m Solar Telescope on La Palma and the *Hinode* satellite during a joint campaign in September 2007. Extremely high-resolution G-band, H $\alpha$ , and Ca II H filtergrams, Fe I and Na I magnetograms, EUV raster scans, and X-ray images show that the emerging region was associated with chromospheric, transition region and coronal brightenings, as well as with chromospheric surges. We suggest that these features were caused by magnetic reconnection at low altitude in the atmosphere. To support this idea, we perform potential and linear force-free field extrapolations using the FROMAGE service. The extrapolations show that the emergence site is cospatial with a 3D null point, from which a spine originates. This magnetic configuration and the overall orientation of the field lines above the emerging flux region are compatible with the structures observed in the different atmospheric layers, and remain stable against variations of the force-free field parameter. Our analysis supports the predictions of recent 3D numerical simulations that energetic phenomena may result from the interaction between emerging flux and the pre-existing chromospheric and coronal field.

*Subject headings:* Sun: magnetic fields — Sun: photosphere — Sun: chromosphere — Sun: corona — Sun: activity

### 1. INTRODUCTION

Our understanding of the emergence of magnetic fields through the solar atmosphere has greatly improved over the last years thanks to new observations and numerical models (see, e.g., Fan 2009, and references therein). A large number of complex simulations, including radiative transfer effects and/or extending from the convection zone to the corona, have been carried out in order to shed light on the fate of the flux brought into the atmosphere by magnetic buoyancy, and on its possible interaction with the ambient field already present at the emergence site (e.g., Galsgaard et al. 2007; Martínez-Sykora et al. 2008, 2009; Tortosa-Andreu & Moreno-Insertis 2009).

The interaction between emerging flux regions (EFRs) and the ambient field is usually believed to be responsible for perturbations in the upper atmosphere. As a consequence of the reconnection between the different flux systems, part of the magnetic energy stored in the field lines is converted into heat and part into the kinetic energy of impulsive phenomena, like jets and surges (Yokoyama & Shibata 1995).

Such a reconnection scenario has been investigated

through MHD numerical simulations. They indeed show that the emerging magnetic flux may interact and reconnect with the pre-existing coronal field. The results obtained from the 2D models of Yokoyama & Shibata (1995, 1996) have been confirmed by the more recent 3D models of Archontis et al. (2004, 2005), although the dynamics is significantly more complicated. The models suggest that flux emergence may be a relevant source of energy for the upper atmospheric layers and that magnetic reconnection between the EFR and the pre-existing field can lead to the ejection of chromospheric matter into the corona (Archontis et al. 2005; Isobe et al. 2005; Martínez-Sykora et al. 2009). At the reconnection site the temperature can reach  $1 - 2 \times 10^7$  K, and the plasma is emitted in the form of high-speed ( $> 100$  km s<sup>-1</sup>) jets, at a height of  $\sim 1.5 - 2$  Mm above the base of the corona. The relative orientation between the two interacting flux systems seems to play an important role in the reconnection process, since it strongly influences the efficiency of the energy release and the consequent heating (Galsgaard et al. 2007). However, it ought to be realized that in all these ideal-MHD experiments reconnection occurs due to numerical resistivity, which is still several orders of magnitude larger than the physical resistivity of the solar plasma.

From an observational point of view, episodes of magnetic flux emergence are often accompanied by highly energetic phenomena in the chromosphere, like Ellerman bombs (EBs) and H $\alpha$  and H $\beta$  surges. EBs, discovered by Ellerman (1917), are small-scale brightenings observed in the wings of chromospheric lines, such as H $\alpha$  or Ca II H. They have elliptical shapes and a typical size of

salvo.guglielmino@oact.inaf.it

<sup>1</sup> Dipartimento di Fisica e Astronomia, Università di Catania, I 95123 Catania, Italy

<sup>2</sup> Instituto de Astrofísica de Andalucía (CSIC), Apdo. de Correos 3004, E 18080 Granada, Spain

<sup>3</sup> LESIA, Observatoire de Paris, CNRS, UPMC, Université Paris Diderot, 5 place Jules Janssen, 92190 Meudon, France

<sup>4</sup> Mullard Space Science Laboratory, RH5 6NT Holmbury St. Mary, Dorking, Surrey, UK

<sup>5</sup> Max-Planck-Institut für Sonnensystemforschung, D 37191 Katlenburg-Lindau, Germany

$\sim 1''$  (Georgoulis et al. 2002).  $H\alpha$  surges are straight or curved ejections of plasma with a filamentary structure. They may extend for up to  $1-2 \times 10^5$  km, reaching velocities of some tens of  $\text{km s}^{-1}$  (Kurokawa & Kawai 1993). EBs and surges have energies of the order of  $10^{28}$  erg and lifetimes of 10 – 20 minutes. They are thought to share a common origin in the ejection of chromospheric matter (e.g., Matsumoto et al. 2008).

In multiwavelength observations these features have been associated both in time and in space with coronal events found at flux emergence sites, such as UV/EUV brightenings (Chae et al. 1999; Yoshimura et al. 2003) and X-ray jets (Shibata et al. 1992). Although several authors studied the relationship between surges and X-ray brightenings, the existence of a clear correlation is disputed. For instance, Canfield et al. (1996) observed an X-ray jet spatially separated from a surge, whereas Zhang et al. (2000) found an X-ray jet during the late stages of an  $H\beta$  surge. On the other hand, it has been noticed that before the occurrence of a flare, coronal lines may show small-scale brightenings and non-thermal broadenings, which can be caused by magnetic reconnection, where flux is emerging and canceling (Wallace et al. 2010).

Recent observations have confirmed the results of MHD simulations in greater detail. Liu & Kurokawa (2004) presented a multiwavelength analysis of a chromospheric surge from the photosphere to the corona that supports the idea of magnetic reconnection in the low chromosphere. Also the high-resolution study of Brooks et al. (2007), analyzing  $H\alpha$  surges produced by the collision of small-scale magnetic flux concentrations of opposite polarity (moving magnetic features) around sunspots, showed that the chromosphere is heated up to coronal temperatures during magnetic field reconnection, in agreement with the findings of Yokoyama & Shibata (1996). Furthermore, Moreno-Insertis et al. (2008) carried out a numerical simulation of flux emergence which reproduced the three-dimensional structure of X-ray jets observed in coronal holes with the X-Ray Telescope (XRT; Golub et al. 2007) and the Extreme Ultraviolet Imaging Spectrometer (EIS; Culhane et al. 2007) aboard the *Hinode* satellite (Kosugi et al. 2007).

Despite these findings, the relationship between the evolution of emerging magnetic fields and the fine structure of  $H\alpha$  surges, Ca II and EUV brightenings, and X-ray jets still has to be clarified. Small-scale changes in the topology of the emerging flux may lead to a dynamic energy release, so high-resolution observations are needed to shed some light on this issue.

Here we present a multi-wavelength analysis of extremely high spectral, temporal, and spatial resolution observations of a small-scale EFR, obtained during a coordinated campaign between the Swedish 1-m Solar Telescope (SST; Scharmer et al. 2003) and *Hinode*. In a previous paper (Guglielmino et al. 2008), we used a subset of Ca II H filtergrams, Na I D1 magnetograms, and Fe I 630.2 nm spectropolarimetric scans taken by *Hinode*'s Solar Optical Telescope (SOT; Tsuneta et al. 2008) to study the rapid evolution of the EFR. Initially, the EFR showed upflows with horizontal magnetic fields in the central part and downflows with vertical field lines near the footpoints. As the magnetic flux increased, strong

Ca II H brightenings were detected at the contact line between the positive polarity of the EFR and a network element of opposite polarity, without clear counterparts in the G band. We interpreted these brightenings as the signature of chromospheric heating caused by the magnetic reconnection of the two flux systems.

Here we study the same EFR in the upper atmosphere, basing our analysis on the Ca II H and  $H\alpha$  observations acquired at the SST and the simultaneous measurements of XRT and EIS. These observations provide the most complete view of a flux emergence event ever obtained, as they cover all the atmospheric layers from the photosphere to the corona at the highest spatial resolution achievable with current telescopes.

We also perform a series of potential and linear force-free field (LFFF) extrapolations of the photospheric magnetograms to study the topology of the coronal field at the site of emergence and the interactions between the EFR and the ambient field during the emergence process.

In the next sections we describe the observations and the data reduction (Sect. 2), the evolution of the EFR at different heights (Sect. 3), and the topology of the magnetic field (Sect. 4). In Sect. 5 we suggest that the observed phenomena were caused by magnetic reconnection at low altitude in the solar atmosphere.

## 2. OBSERVATIONS AND DATA ANALYSIS

The data analyzed in this paper were acquired during the *Hinode* Operation Plan 14, a joint campaign between the solar telescopes of the Canary Islands and *Hinode*. On 2007 September 30, the active region NOAA 10971 located at heliocentric coordinates ( $178''$ ,  $-61''$ ) was simultaneously observed with the SST and all the instruments aboard *Hinode*.

The SST followed the active region from 8:45 to 10:05 UT, with a small gap between 9:31 and 9:36 UT. The observations were stopped when the seeing conditions became worse. Ca II H ( $\lambda = 396.85$  nm) and G-band ( $\lambda = 430.56$  nm) images were recorded simultaneously, covering a field of view (FOV) of  $63'' \times 64''$  with a pixel size of  $0.0338''$ . The full width at half maximum (FWHM) of the Ca II H and G-band filters was 0.11 nm and 1.2 nm, respectively. At the same time, the Solar Optical Universal Polarimeter (SOUP; Title & Rosenberg 1981) acquired filtergrams in the core of the  $H\alpha$  line ( $\lambda = 656.29$  nm), together with high-resolution photospheric longitudinal magnetograms. The latter were derived from Stokes  $I$  and  $V$  measurements in the blue wing of Fe I 630.25 nm, at  $\Delta\lambda = -5$  pm. The pixel size of the SOUP filtergrams is  $0.0651''$  and the FOV covers  $63'' \times 60''$ . Additionally, broad-band images were recorded in the continuum of the Fe I and  $H\alpha$  lines to facilitate the alignment of the different datasets.

The observations were corrected for dark current and flat field before being processed with the Multi-Object Multi-Frame Blind Deconvolution technique (MOMFBD; van Noort et al. 2005). As a result, two time series of restored G-band and Ca II H filtergrams with a cadence of 10 s were obtained, together with two time series of restored  $H\alpha$  images and Fe I magnetograms with a cadence of one minute. Further details about the MOMFBD processing can be found in van Noort & Rouppe van der Voort (2008). Thanks to the adaptive optic system of the SST and the MOMFBD

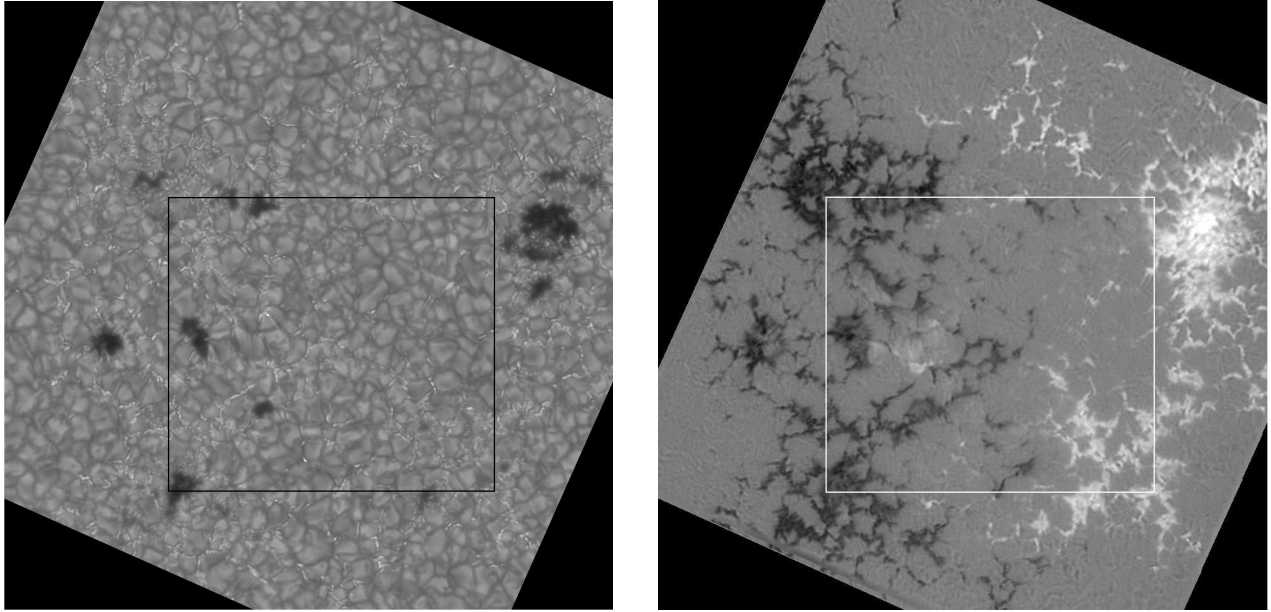


**Figure 1.** SST observations of NOAA 10971 on 2007 September 30 at 9:45 UT. *Left:* G-band filtergram, *Right:* Fe I magnetogram. The squares indicate the part of the FOV shown in Fig. 3. Throughout the paper, North is up and West to the right.

restoration, the spatial resolution of  $0''.2$  achieved at 630.2 nm is very close to the diffraction limit of the SST. Finally, the individual filtergrams were corrected for image rotation, co-aligned, and destretched. Figure 1 displays the entire FOV of a sample SST G-band image and a simultaneous Fe I magnetogram showing NOAA 10971.

The SST observations provide continuous coverage of the lower solar atmosphere. The G-band filtergrams trace the deep photosphere, while the Fe I 630.25 nm measurements represent layers 150 – 300 km above  $\tau = 1$  (e.g., Cabrera Solana et al. 2005). The Ca II H line forms at a temperature of  $\sim 10000$  K (low chromosphere), and the H $\alpha$  line at  $\sim 15000$  K (mid-chromosphere; see, e.g., Vernazza et al. 1981).

The method of analysis of the SOT data is discussed in Guglielmino et al. (2008). As regards other *Hinode* observations, we have used the *SolarSoft* IDL package to obtain Level-1 data. An area of  $100'' \times 240''$  was scanned by EIS with an exposure time of 25 sec per slit position, using the  $2''$  wide slit. The pixel size is then  $1'' \times 2''$ , with the larger size along the (EW) scan direction. Eight raster scans of the active region were performed from 8:20 to 9:50 UT and from 10:20 to 11:50 UT, each one with a duration of  $\sim 22$  minutes. The deep exposures allow the detection of very weak signals, such as those expected in the quiet Sun. The spectral ranges covered by the observations contain a number of cool and hot emission lines (see Table 1). The resolving power of EIS at these wavelengths is 3000 – 4000, as described by Young et al. (2007).

The EIS data were calibrated with the help of standard *SolarSoft* procedures. In particular, we used the routine `eis_prep`, which corrects for hot pixels and other bad data points and converts DN values into intensities in units of  $\text{erg cm}^{-2}\text{s}^{-1}\text{sr}^{-1}\text{\AA}^{-1}$ . The EUV spectra were corrected for the slit tilt and thermal drift using the `eis_wave_corr` routine. The long-wavelength detector was aligned with respect to the short-wavelength detec-

tor using a fixed displacement of 1 pixel in the  $x$ -direction and 13 pixels in the  $y$ -direction, using the Fe XII 195.12  $\text{\AA}$  radiance map as a reference. Moreover, we adopted the  $\lambda$ -dependent correction in the  $y$ -direction discussed by Young et al. (2009), to whom we refer for further details about the EIS data calibration.

In order to extract line parameters from the EIS spectra, we implemented the MPFIT *SolarSoft* procedures into the `fit_line` routine, to automatically fit the calibrated spectra with Gaussians. In normal conditions, a Gaussian function is found to be a reasonable approximation to the line profiles (e.g., Mariska et al. 2007). The procedure allows the user to select the transition of interest and the corresponding wavelength range, and to deduce the integrated emission intensity (radiance), the background level (i.e., the continuum), the line centroid, and the FWHM. The Doppler velocity  $v_D$  can be easily calculated as

$$v_D = c \frac{\lambda - \lambda_0}{\lambda_0}, \quad (1)$$

where  $c$  represents the speed of light,  $\lambda$  is the position of the line centroid obtained from the fit, and  $\lambda_0$  is the rest wavelength of the transition. The values of  $\lambda_0$  are extracted from the CHIANTI atomic database (Landi et al. 2006; Dere et al. 1997), as listed by Brown et al. (2008). The non-thermal velocity  $v_{\text{non-th}}$  was calculated by means of the `eis_width2velocity` routine, which removes the instrumental width  $W$  and the known thermal velocity  $v_{\text{th}}$  of the line from the observed FWHM, using the relation

$$\text{FWHM}^2 = W^2 + 4 \ln 2 \frac{\lambda^2}{c^2} (v_{\text{th}}^2 + v_{\text{non-th}}^2) \quad (2)$$

(Harra et al. 2009). The uncertainties in Doppler shift and FWHM correspond to the formal errors of the Gaussian fit.

To derive the electron density we used a line ratio technique. The intensity ratio of density-sensitive line pairs

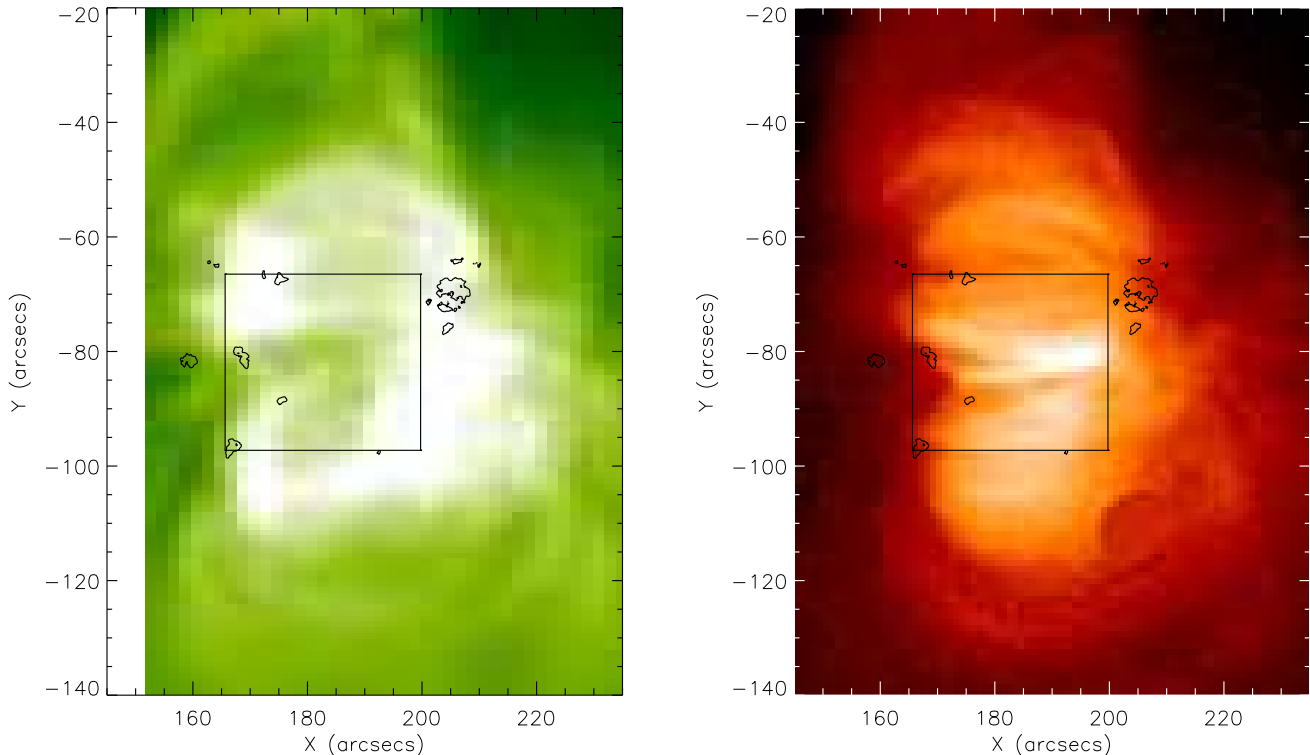


**Figure 2.** *Hinode* observations of NOAA 10971 at 9:45 UT. *Left:* map of radiance in Fe XII 195.12 Å from the EIS raster scan started at 9:27 UT, *Right:* X-ray intensity through the C/polyimide filter. Both maps are shown in logarithmic scale, with the number of counts ranging from 0.05 to 3500 for EIS and from 10 to 2000 for XRT. The contours mark the position of the pores seen in the G band (Fig. 1), and the squares indicate the part of the FOV displayed in Fig. 3.

is governed by the populations of the energy levels of the ion. The populations vary with the rate of ion-electron collisions, which depends on the electron density (for more details, see Phillips et al. 2008). The relationship between the line ratio and the density was calculated using the CHIANTI database.

X-ray images were acquired through the Carbon polyimide (C/poly), the Be thin, and the Be thick filters of *Hinode*/XRT, with exposure times of 1.03, 23 and 46 s, respectively. The cadence of the XRT observations is 82 s. These measurements cover a FOV of  $384'' \times 384''$  with a pixel size of  $1''$ . They have been corrected for dark current, CCD bias, and cosmic rays using the `xrt_prep` routine. The contamination spots have been identified and removed by means of the `xrt_tup_contam` procedure, and finally the images have been corrected for pointing jitter. Figure 2 shows NOAA 10971 as observed by EIS in the coronal Fe XII 195.12 Å line and by XRT through the C/poly filter.

### 2.1. Co-alignment of the observations

A critical step in multi-instrument observations is the precise co-alignment of the different datasets. Small offsets may also exist between images taken at different wavelengths with the same instrument. The internal offsets of SOT were evaluated by Shimizu et al. (2007) for the Broadband Filter Imager, while only pre-launch data are available for the Na I line observed with the Narrowband Filter Imager.

The monochromatic images of each temporal series acquired at the SST were aligned with respect to a reference time image using cross-correlation techniques. To

coalign the SOT and the SST images, we used the G-band filtergrams from both instruments at the reference time (9:30 UT), resampled to a pixel size of  $0.055''$ . The displacement between them was obtained by cross-correlation, using the pores present in the FOV as fiducial points. The same shift was applied to the simultaneous SST Ca II H images. To align the SST  $H\alpha$  filtergrams and Fe I magnetograms, we cross-correlated the SOT G-band filtergrams with the images taken in the continuum of the  $H\alpha$  and Fe I lines. We estimate the accuracy of this procedure to be on the order of  $\pm 0'.1$ .

Unfortunately, the pointing information stored in the *Hinode* FITS files is not sufficient to determine the offsets between XRT, EIS, and SOT. Thus, we aligned the XRT filtergrams with respect to the SST  $H\alpha$  channel. We compared the  $H\alpha$  images with the XRT images, and not with the EIS scans, because the latter do not represent instantaneous snapshots and also because their spatial resolution is worse. The XRT image was superimposed on the corresponding  $H\alpha$  filtergram by means of the *iTools* IDL package. This application handles the image transparency and is very useful to check the correspondence of common structures, such as loops and bright regions. In particular, we aligned the X-ray coronal loops with the high-resolution  $H\alpha$  features looking for a good overlap between them and for a position of the X-ray loops compatible with the endpoints observed in  $H\alpha$ . The alignment accuracy is comparable to the pixel size of XRT, i.e.,  $1'' - 2''$ .

Finally, using cross-correlation and *iTools* again, we superimposed the EIS Fe XII 195.12 Å coronal intensity map on the aligned XRT image, finding the location of

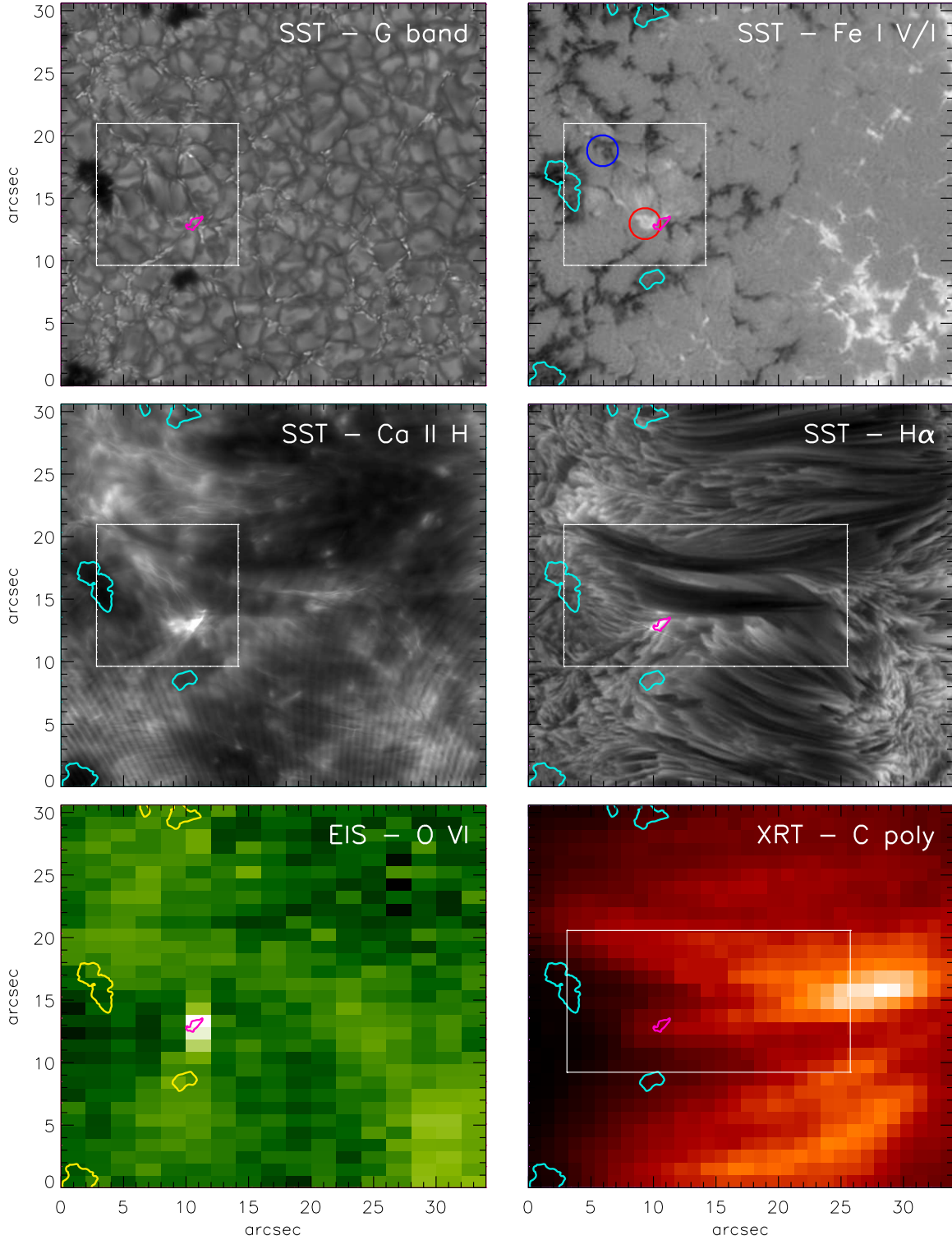


**Figure 3.** EFR as observed at 9:45 UT, when it shows clear signatures in all the layers of the solar atmosphere. Displayed are a G-band filtergram (*top left*), a Fe I magnetogram (*top right*), a Ca II H line core filtergram (*middle left*), and an H $\alpha$  line core filtergram (*middle right*), all acquired at the SST. The bottom panels show the intensity of the O VI 184.12 Å line from the EIS raster scan started at 9:27 UT (*left*) and the X-ray intensity through the XRT C/polyimide filter (*right*). The square, with a FOV of  $\sim 12'' \times 12''$ , indicates the location of the EFR analyzed here. The emerging positive (negative) polarity is indicated with a red (blue) circle in the Fe I magnetogram. For comparison, we overplot light blue (yellow on the EIS image) contours over a certain threshold of the G-band intensity to mark the location of the pores as seen in the photosphere, whereas purple contours indicate the site of the Ca II H brightening. On the H $\alpha$  and X-ray images we overplot a rectangle with double size ( $\sim 24'' \times 12''$ ), to encompass the elongated chromospheric surge and the X-ray loop. The time sequences of G-band, Fe I, Ca II H and H $\alpha$  measurements are available as animations in the online journal (AR10971\_20070930\_Gband.mov, AR10971\_20070930\_FeI6302.mov, AR10971\_20070930\_CaII.mov, AR10971\_20070930\_Halpha.mov, respectively). In the movies, major tick marks are separated by  $10''$ . They show the same FOV, except the H $\alpha$  one which has a larger FOV in the horizontal direction to accommodate the surges. The contours represent the visible borders of the pores.

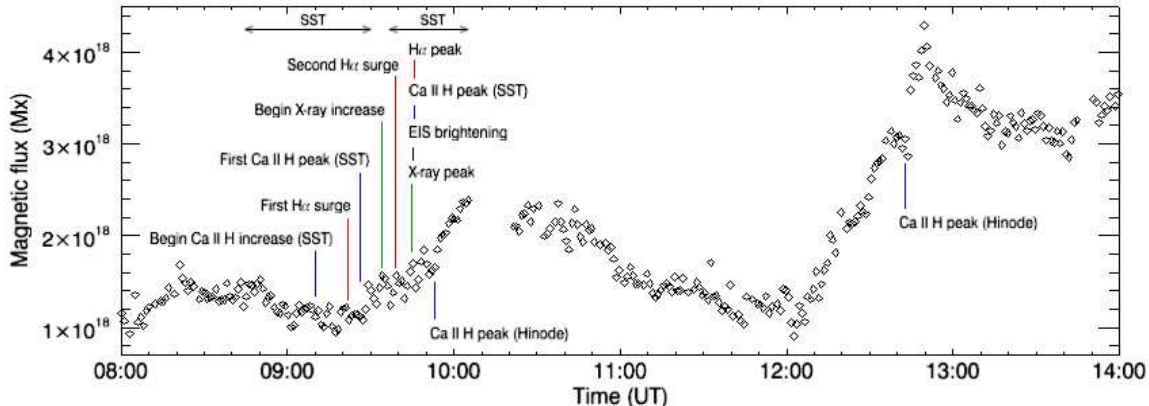


**Figure 4.** Long-term evolution of the positive magnetic flux brought by the EFR, as computed from the *Hinode* Na I D1 magnetograms. The associated events are marked with labels. The horizontal segments indicate the periods with SST data.

the EIS measurements with a precision of the order of  $2'' - 3''$ .

### 3. RESULTS

An EFR appeared at about 8:00 UT at the internal edge of the main negative polarity of active region NOAA 10971 (see Guglielmino et al. 2008). With a length of  $\sim 8$  Mm and a total photospheric flux of  $1.4 \times 10^{19}$  Mx, this EFR classifies as a small ephemeral region.

Figure 3 shows the EFR and its surroundings at 9:45 UT, from the photosphere (SST G-band filtergram) to the low corona (*Hinode* XRT C/poly filtergram). It represents a global view of the emergence event in all the atmospheric layers covered by our observations.

The emergence of new flux into the photosphere is clearly seen in the magnetograms taken by *Hinode*/SOT and the SST. Figure 4 displays the evolution of the positive magnetic flux in the upper photosphere as deduced from the Na I D1 589.6 nm measurements of *Hinode* (Guglielmino et al. 2008). There were two main episodes of flux emergence, beginning at around 9:20 UT and 12:00 UT. Only the former is covered by the SST observations. Marked in the same figure are a number of events associated with the emergence process: brightenings in the chromospheric Ca II H and H $\alpha$  lines, H $\alpha$  surges, and transient enhancements in cool EUV lines and X-rays. All these phenomena were observed during the first increase of the flux and span a broad range of heights in the solar atmosphere. Below we describe them in more detail.

#### 3.1. Flux emergence in the photosphere

The temporal sequence displayed in Fig. 5 summarizes the evolution of the EFR during the simultaneous observations of *Hinode* and the SST. A comparison between the G-band images (*first column*) and the magnetograms (*second column*) initially shows bright points (BPs) at the position of the stronger flux patches of the EFR. As new flux emerges, transient darkenings appear along the direction connecting the two main flux concentrations (see, e.g., the third and seventh rows). These dark lanes have a length of  $3'' - 4''$  and show BPs at their endpoints. Interestingly, a dark lane is visible in the continuum in the *Hinode* spectropolarimetric scan taken at

09:18 UT, associated with upflows and horizontal fields (Guglielmino et al. 2008).

The granulation pattern is also disturbed: the granular structures between the two polarities of the EFR become larger and more elongated than is typical in the quiet Sun, reaching a size of about  $6 \text{ Mm}^2$ , almost twice as large as normal granular cells (see, e.g., the structure outlined by the green contour in the G-band image at 9:47 UT). The granules fragment after growing for  $\sim 10$  minutes.

We have calculated the horizontal expansion velocity of the anomalous granules using the Local Correlation Technique (LCT; see November & Simon 1988). The algorithm was applied to two subsets of SST G-band images, from 9:15 to 9:30 UT and from 9:37 to 9:52 UT, adopting a FWHM window of  $5 \times 5$  pixels ( $0''.17 \times 0''.17$ ) and a time interval of one minute. In Fig. 6 we display the horizontal velocity field obtained for the first subset, indicating the direction and magnitude of the motion with arrows. The average speed is about  $3 \text{ km s}^{-1}$ , with a peak of about  $4 \text{ km s}^{-1}$  near the BPs associated with the positive polarity of the EFR. We also recognize diverging motions from the center of the EFR toward the boundaries of the anomalous granules. These motions concentrate the magnetic field in the network patches observed around the EFR.

The dynamics revealed by our data confirms the findings of Strous & Zwaan (1999), now at smaller spatial scales. Similar dark lanes were detected previously by Otsuji et al. (2007) in *Hinode* G-band and continuum images of an EFR that showed dark Ca II H filaments. Transient darkenings and abnormal granulation have also been reported by Cheung et al. (2008).

Our observations support the results of the numerical simulations of Cheung et al. (2007, 2008) and Tortosa-Andreu & Moreno-Inertis (2009) concerning the photospheric evolution of EFRs. We indeed find upward velocities of  $1.5 \text{ km s}^{-1}$  associated with strong horizontal fields of  $\sim 1.5 \text{ kG}$  (Guglielmino et al. 2008). However, there are some differences: for instance, the size reached by the anomalous granules is smaller than the simulated granules by at least a factor of 2.

We also note that the EFR is not formed by the emergence of a pair of coherent flux concentrations of op-

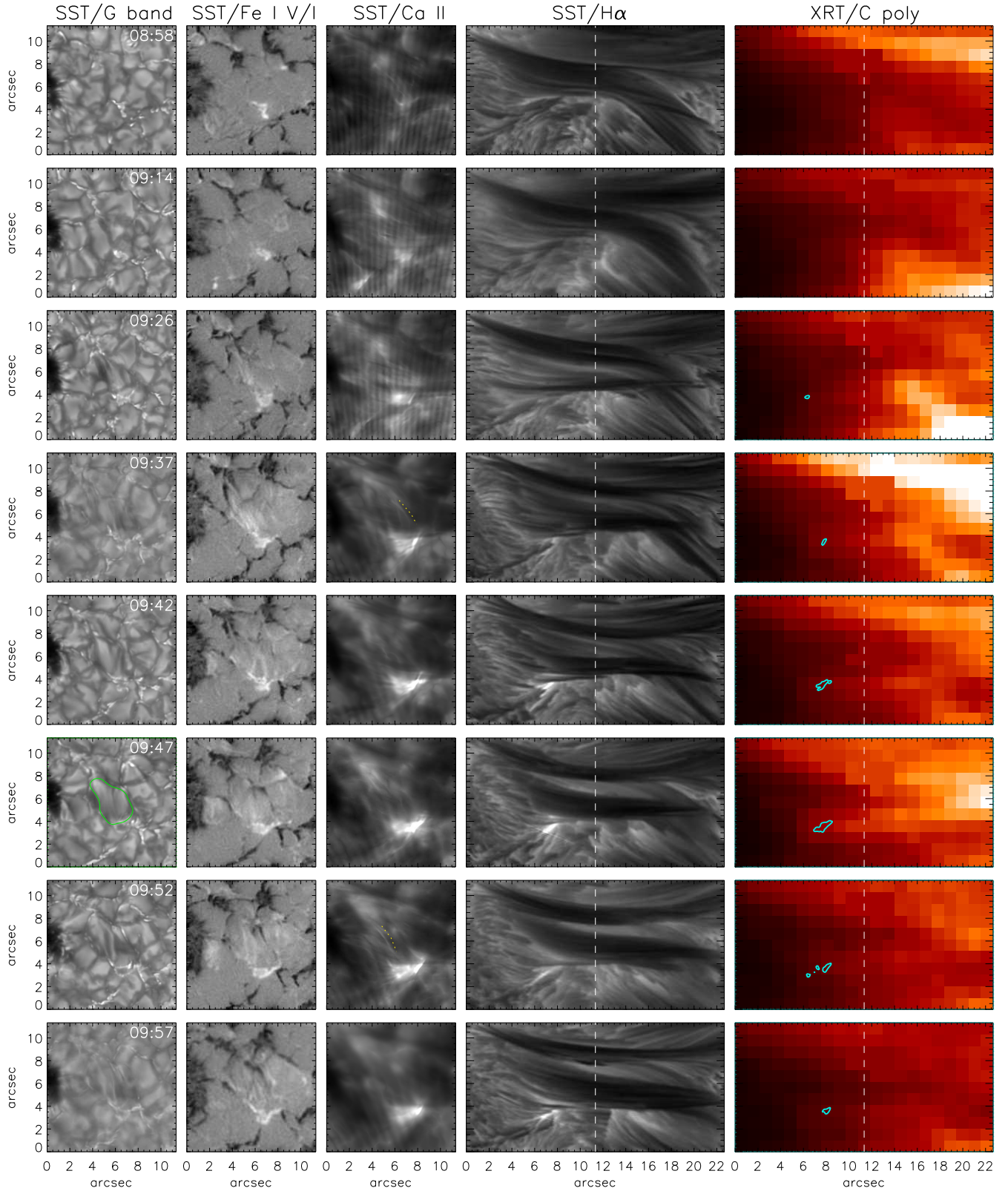


**Figure 5.** Temporal evolution of the EFR between 8:58 and 9:57 UT. Displayed are simultaneous G-band filtergrams (*first column*), Fe I magnetograms (*second column*), Ca II H and H $\alpha$  filtergrams (*third and fourth columns*), acquired at the SST, and XRT C/poly images (*fifth column*), showing the EFR in the various atmospheric layers. The color tables are rescaled to the maximum intensity for each column. The FOV covers the squared/rectangular regions highlighted in Fig. 3. The left half of the H $\alpha$  and X-ray images contains the FOV displayed in the other filtergrams. For comparison, blue contours in the X-ray filtergrams indicate the location of the Ca II H brightenings. The strong H $\alpha$  brightening and the enhanced emission of the X-ray loop cospatial to the Ca II H brightening are clearly visible. At 9:47 UT the green contour in the G-band image indicates an anomalous granular cell at its maximum size. To help identify the fibrils that connect the two polarities of the EFR in the chromosphere, we have drawn yellow dotted lines parallel to them in some of the Ca II H panels.

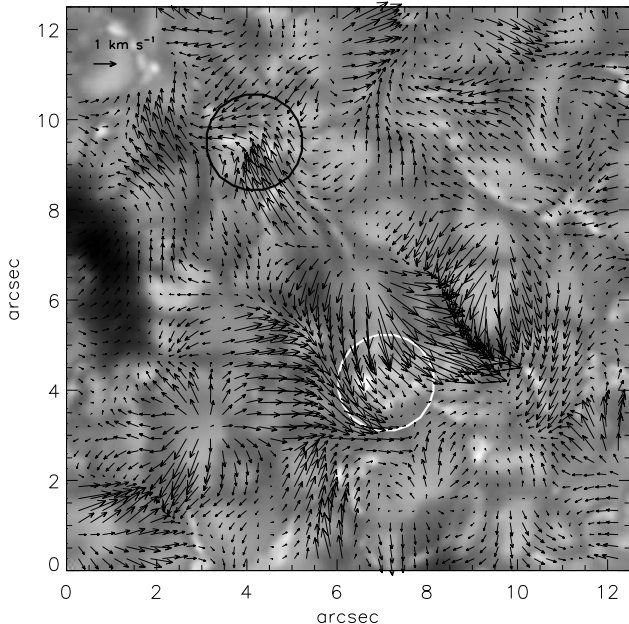


**Figure 6.** Horizontal velocity field (15 minutes average from 9:15 to 9:30 UT), as derived by the LCT technique, overplotted on a SST G-band image acquired at 9:23 UT, with a FOV of  $25'' \times 25''$  centered on the EFR. The arrows indicate the direction and the magnitude of the horizontal velocity. The arrow in the left-top corner represents a velocity of  $1 \text{ km s}^{-1}$ . The circles mark the position of the two main polarities of the EFR.

posite polarity. Rather, the flux appears as a series of small patches with mixed polarities, even if the EFR shows a net bipolarity (see the Fe I movie in the online Journal). Such a pattern is extremely reminiscent of the sea-serpent shape of the emerging field lines seen in the simulations.

### 3.2. Effects in the upper atmospheric layers

Figure 5 shows that the EFR produced localized brightenings in the chromospheric Ca II H and H $\alpha$  lines. They were first detected at 09:27 UT and 09:39 UT, respectively. The brightenings have an elliptical shape, with a width of  $\sim 0''.15$  and a length of  $\sim 0''.7$ , corresponding to about  $100 \times 500 \text{ km}^2$ .

In the Ca II H images (third column of Fig. 5), the connectivity between the two polarities of the EFR is revealed by narrow bright filaments that join them and change continuously with time (see frames 355-370 in the accompanying Ca II movie). The thickness of these filaments is about 2 – 3 pixels, corresponding to  $\sim 0''.08$ , right at the diffraction limit of the telescope. They are not to be confused with the interference fringes aligned in nearly North-South direction, arising from imperfect flatfield correction and amplified by the MOMFBD process<sup>6</sup>. This connectivity is not observed in the higher atmospheric layers, probably because of the dominance of larger scale structures (see the H $\alpha$  and the C/poly filtergrams in the fourth and fifth columns of Fig. 4).

The structure and the temporal evolution of the chromosphere is clearly visible in the Ca II H movie. Plasma flows seem to be present in the region around the EFR,

<sup>6</sup> We note that the only effect of such fringes is to increase the noise of the intensity measurements.

and the brightening just lies where some of these flows are converging.

Three chromospheric surges, associated with the EFR and cospatial with some Ca II H plasma flows, are recognized in the SST H $\alpha$  images starting at 9:23, 9:37, and 9:52 UT. The surges appear southward of an arch filament system (AFS) connecting the opposite polarities of the active region. The loops of the AFS show continuous morphological variations and their footpoints are anchored in the magnetic network outlining the boundaries of supergranular cells (see Fig. 1). The lack of spectroscopic information does not allow us to estimate the downflow/upflow motions and the plasma speed in the loops, which is usually reported to be on the order of  $10 - 15 \text{ km s}^{-1}$  (Zuccarello et al. 2009).

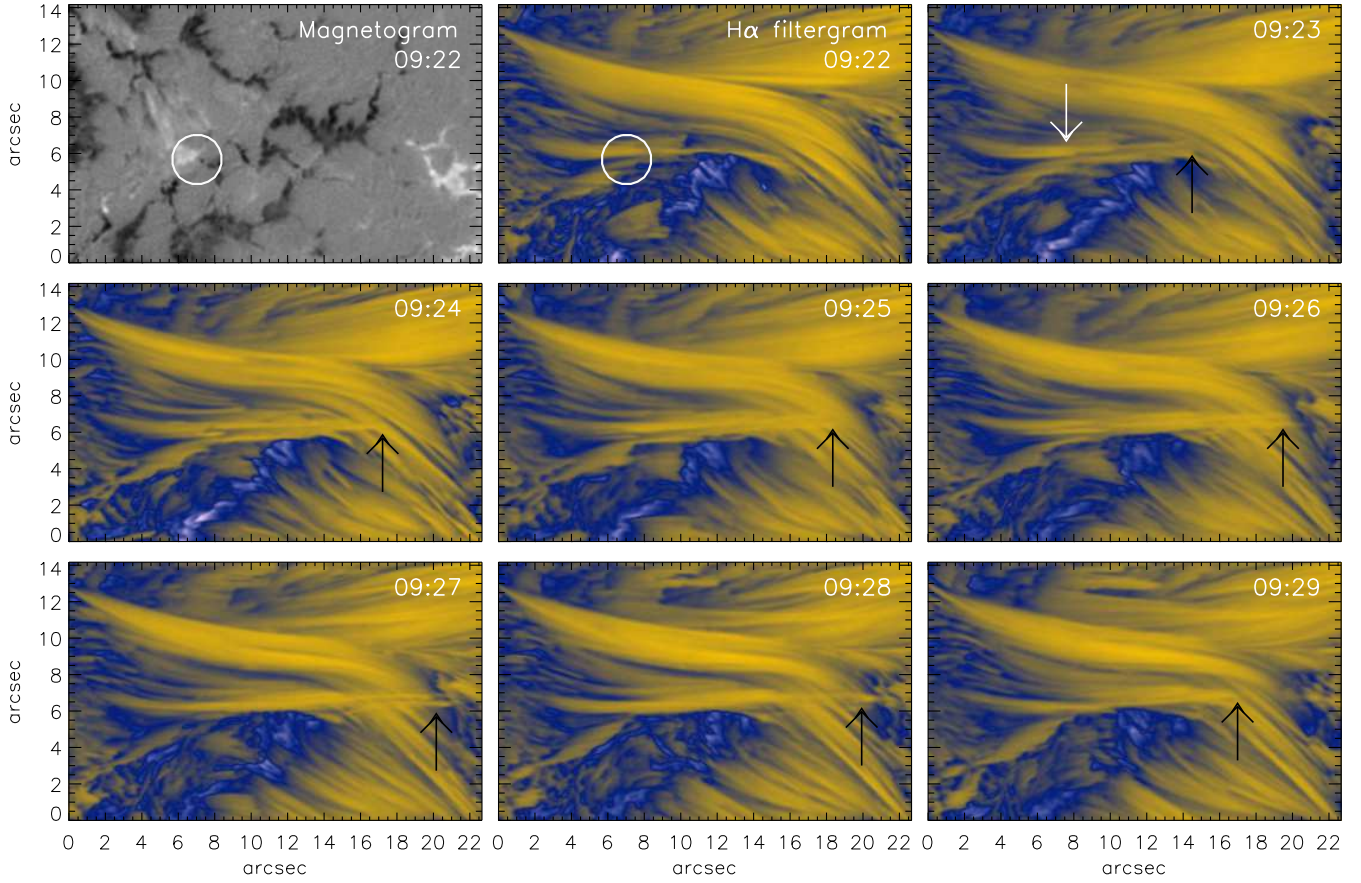
The temporal sequence of H $\alpha$  images displayed in Fig. 7 shows the evolution of the first chromospheric surge with enhanced colors<sup>7</sup>. To facilitate comparisons, the initial photospheric magnetogram is given in the first panel. Thanks to the extremely high spatial resolution of the measurements, the filamentary structure of the surge is clearly visible. A Y-shaped feature at the base of the surge is recognized at 9:23 UT (indicated by the white arrow). At 9:40 UT, its cross-point location coincides with the site of the H $\alpha$  and Ca II H brightenings (compare the fourth and fifth rows of Fig. 5).

The sharp edge of the surge allows us to estimate the projection of its velocity in the horizontal direction. To that end we have considered the distance between the centroid of the EFR and the west edge of the surge: there is an initial impulsive phase during which the distance increases (9:23 – 9:28 UT), followed by a decay phase (9:29 – 9:30 UT). We have performed a parabolic fit to the impulsive phase: the (projected) speed after the first minute of the ejection is  $53 \text{ km s}^{-1}$ , whereas the average speed during the impulsive phase is  $34 \text{ km s}^{-1}$ , in agreement with previous estimates (e.g. Brooks et al. 2007). The uncertainty of these values is about  $\pm 2 \text{ km s}^{-1}$ .

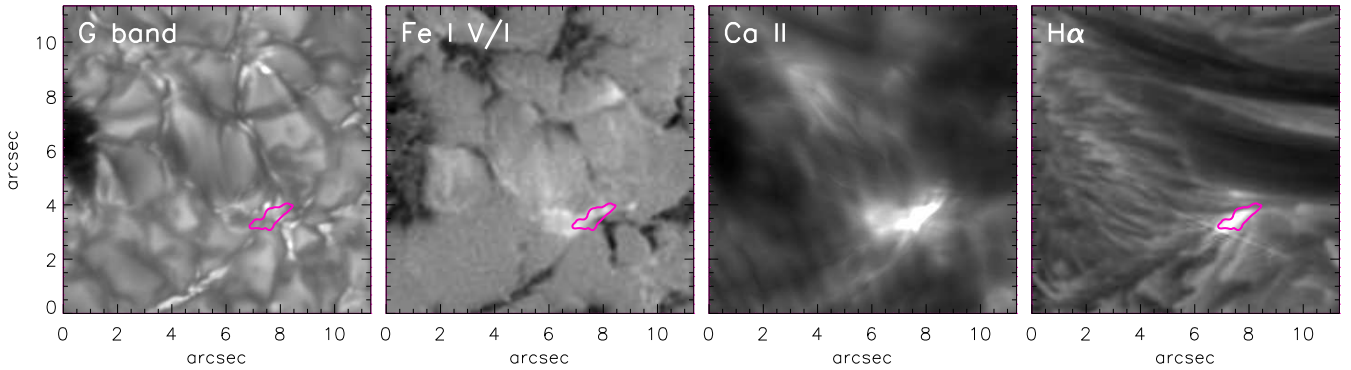
Figure 8 is a close-up of the 9:47 UT observations displayed in Fig. 5. It shows that the Ca II H and H $\alpha$  brightenings occurred in the contact region between the emerging positive polarity and a pre-existing network element of negative polarity. Contours indicating the maximum Ca II H line-core intensities are overplotted for reference. BPs can be seen at the position of the small-scale flux patches, but there are no indications of any heating process around the contact line in the photospheric G-band filtergrams.

Figure 5 shows that the site of the Ca II H brightening coincides with the footpoint of an X-ray loop with enhanced emission, which could be a jet. Coronal variations during the emergence event were observed only in the images taken with the C/poly filter. This filter is sensitive to temperatures down to  $\log T = 6$ , while the thin and thick Be filters react to much hotter temperatures (Golub et al. 2007). Thus, it appears that the energy released during the emergence process was not sufficient to heat the plasma well above  $\sim 10^6 \text{ K}$ .

<sup>7</sup> The second and third surges are smaller and more difficult to identify, hence we will not consider them further. However, we note that the third surge appears to be associated with a strong H $\alpha$  brightening that peaked at 9:50 UT, some  $2''$  north of the main brightening of Fig. 3.



**Figure 7.** Time sequence of H $\alpha$  line core filtergrams, showing the development of the first surge associated with the EFR. The images have a cadence of one minute. For comparison, the first panel shows the Fe I magnetogram corresponding to the first H $\alpha$  image (9:22 UT). The sharp boundary of the chromospheric surge (black arrows) allows us to easily follow the temporal evolution of the structure. The white arrow indicates the Y-shaped structure seen since the initial stages of surge. A full animation including this and the other surges can be found in the online Journal.



**Figure 8.** EFR as observed in the photosphere/chromosphere at 9:47 UT. The FOV is the same as in Fig. 5. Purple contours indicate the site of maximum Ca II H intensity. As can be seen, the Ca II H and H $\alpha$  brightenings coincide with BPs and with the contact region of the approaching polarities.

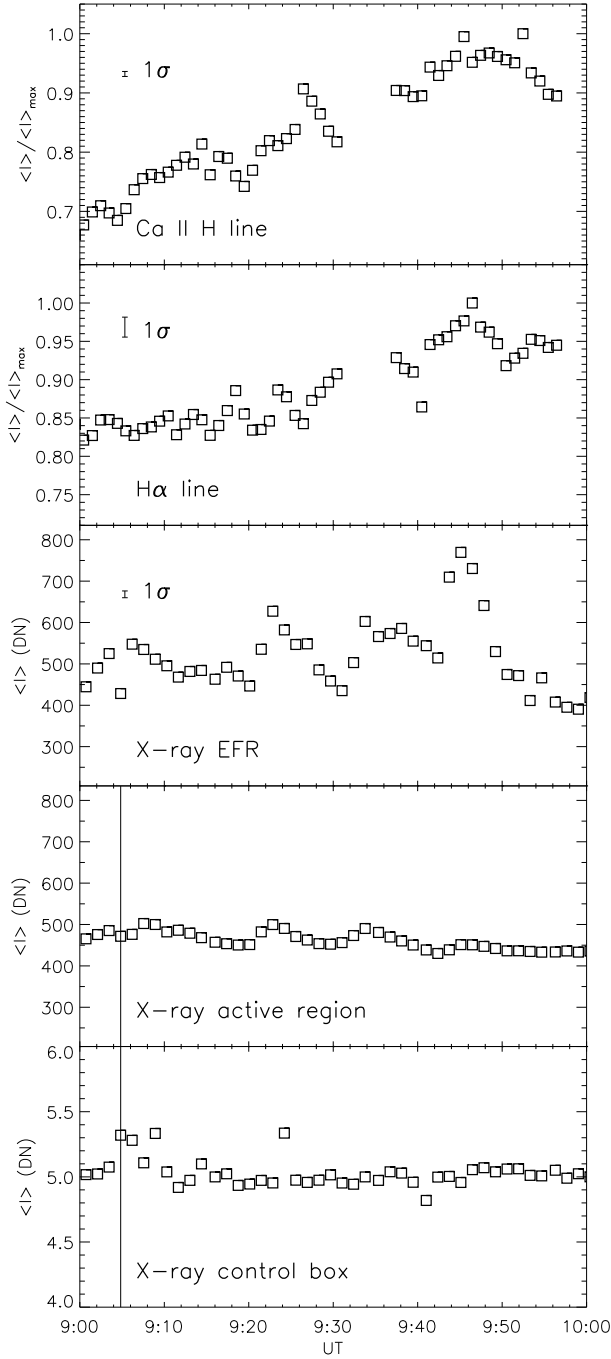


**Figure 9.** Temporal evolution of the Ca II H and H $\alpha$  intensities, normalized to their maximum value, and the X-ray intensities (EFR, active region, and control box). There was a simultaneous peak in the Ca II, H $\alpha$ , and X-rays curves around 9:45 UT. The vertical lines in the X-ray plots indicate the time when *Hinode* left the South Atlantic Anomaly. The  $1\sigma$  marks indicate the amplitude of the error bars.

We plot in Fig. 9 the temporal evolution of the maximum Ca II H, H $\alpha$ , and X-ray brightness at the emergence site<sup>8</sup>. The Ca II H intensity and later the H $\alpha$  in-

<sup>8</sup> To obtain these values, in each frame we have averaged the four pixels of maximum intensity within a  $5'' \times 5''$  box centered on the positive polarity patch of the EFR. The box is the same for all the data sets.

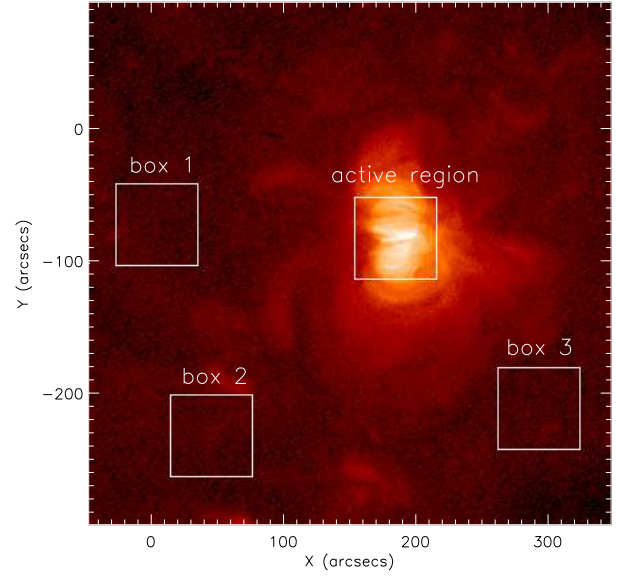


**Figure 10.** Full FOV of the XRT measurements with the C/polyimide filter at 9:45 UT. The maps is shown in logarithmic scale between 1 and 2000 counts. The box containing the active region and the three boxes used for the plots in Fig. 9 are shown. All the boxes have a size of  $63'' \times 63''$ .

tensity show a continuous increase beginning at 9:05 and 9:27 UT, respectively, whereas the X-ray enhancement is more abrupt. Despite this difference, the maximum X-ray intensity was observed at the time of the strongest Ca II H and H $\alpha$  brightenings (around 9:45 UT). In Fig. 9 we also display the mean X-ray intensities within a box containing the entire active region (see Fig. 10). It looks quite flat, confirming that the X-ray increase in the EFR was not associated with a general increase of the background emission in the active region. The bottom panel of Fig. 9 shows the mean XRT intensity in the three control boxes of Fig. 10. This curve demonstrates that the X-ray enhancements in the EFR were solar in origin and not due to variations of the XRT transmission or cosmic ray events, except perhaps for the small peaks seen during the crossing of the South Atlantic Anomaly and a single peak at around 9:25 UT. However, the latter represents a variation of less than 10% in the control box, while in the EFR it corresponds to a variation of 50%. The X-ray peak at 9:45 UT is not associated with any increase in the control box.

### 3.3. *EIS* spectroscopic analysis

Observations taken with EIS fill the gap between the H $\alpha$  and the XRT observations. EIS observed a brightening in the transition region and in the lower corona above the H $\alpha$  brightening at 9:45 UT, during the raster scan started at 9:27 UT.

Figure 11 displays, from top to bottom, radiance, Doppler velocity, and FWHM maps in He II 256.32 Å, O VI 184.12 Å, Mg VII 278.39 Å, Mg VII 280.75 Å, and Fe XII 195.12 Å. For comparison, the bottom row shows the radiance maps obtained during the previous scan, started at 9:05 UT, where the brightenings are totally absent.

Since the brightening was observed at only one slit position  $2''$ -wide, an adjacent slit position to the west is

regarded as unperturbed medium in the following study. EUV enhancements were detected in the full temperature range  $10^{4.7} - 10^{6.1}$  K. One of the most pronounced brightenings occurred in the Mg VII 278.39 Å line: its radiance was 2.5 times brighter than the adjacent background. The variation of the Doppler shift is smaller than the uncertainty of the measurements ( $6 \text{ km s}^{-1}$ ), and thus no significant velocity change was detected. The width of the Mg VII 278.39 Å line increased from  $0.09 \pm 0.01$  Å in the background to  $0.15 \pm 0.02$  Å at the position of the brightening. Assuming an ion temperature of  $10^{5.8}$  K for this line and the EIS instrumental width of  $0.06$  Å, the non-thermal velocity in the brightening is estimated to be  $81 \text{ km s}^{-1}$ , compared to  $34 \text{ km s}^{-1}$  for the background. The observed increase of the FWHM without a net Doppler shift implies unresolved upflows and downflows within the EIS pixel.

In Fig. 12 we plot the observed profiles at the site of the brightening for a sample of EUV lines, before and during the intensity enhancement. For strong emission lines such as Si X 258.37 Å, a Gaussian function reproduces the observed profile within the measurement errors. Weak emission lines exhibit deviations from a Gaussian shape, mainly because of the low signal-to-noise ratio of the spectrum. However, the small enhancements seen in the wings of Mg VII 278.39 Å could also indicate high speed flows at that temperature.

The electron density is derived from the density-sensitive line pair Mg VII 278.39 Å and Mg VII 280.75 Å, in accordance with Young et al. (2007). Even if ionization equilibrium were not reached in the transient brightening, the density diagnostics would not be affected as we use only the ratio of lines from the same ion, which is determined by collisional excitation processes. Since the line ratio technique is based on the total intensity, i.e., the integral of the emission profile, the exact line shape does not affect the density analysis either (Phillips et al. 2008). The estimated electron density at the position of the brightening is  $10^{9.6 \pm 2} \text{ cm}^{-3}$ , which is roughly 2 times as large as the background value of  $10^{9.2 \pm 2} \text{ cm}^{-3}$ . The density increase may be the signature of chromospheric evaporation. It should be noted that the inferred physical quantities are averages over the EIS pixel, hence the real variations could have been larger. The H $\alpha$  filtergrams indeed show that the width of the chromospheric surge was smaller than  $1''$ .

The physical quantities extracted from the other EUV lines are reported in Table 1. The He II 256.32 Å line is blended with three coronal lines in the red wing, but we cannot correct for that<sup>9</sup>. Nevertheless, the results should be reliable, because in disk observations He II 256.32 Å contributes more than 80% to the blend (Young et al. 2007).

The Fe XII 195.12 Å line is one of the hottest in the sample and shows only a faint brightening. Its parameters are consistent with quiet conditions in the corona and do not seem to be affected by the EFR. However, the continuum intensity of the line is strongly enhanced

<sup>9</sup> For instance, we do not have observations in the spectral range 258.69 – 262.65 Å, where the Si X 261.04 Å line provides a fixed intensity ratio with the Si X 256.37 Å line, one of the lines blended with He II 256.32 Å.

at that position, by a factor of 2. This could indicate the presence of plasma with higher temperature than usual.

The other lines show large non-thermal widths and downflows in the brightening, except for the lowest He II 256.32 Å line and Fe XVI 262.98 Å which show upward motions. Given the uncertainty of the velocity measurements, the downflows cannot be regarded as significant. Only the upflows detected in He II 256.32 Å and Fe XVI 262.98 Å are well above the velocity error, but in these cases the brightening is embedded in a region of strong upflows. Thus, it is unclear whether the emergence event produced velocity changes or not.

As can be seen in Fig. 12, the brightness enhancement decreases with the ion temperature, i.e., with increasing height. This confirms the conclusion drawn from the absence of X-ray signals in the hottest XRT filters, namely that the plasma did not reach very high temperatures.

#### 4. ANALYSIS OF THE MAGNETIC CONFIGURATION

In order to obtain information on the coronal connectivity above the EFR, we performed a series of potential and linear force-free field extrapolations. The coronal loops observed in the EUV and X-ray images of Fig. 2 reveal a non-stressed magnetic configuration: no sigmoid structure is evident and the loops in the arcade appear to be parallel to each other. Such a configuration is indicative of a low-energy state that should be well represented by these extrapolations.

We used the BLFFF code from the FRENCH Online MAGNETIC Extrapolations (FROMAGE) service, which is based on the FFT method of Alissandrakis (1981). The magnetic field  $\mathbf{B}$  was computed for  $z > 0$  using  $B_z = B_{\parallel} \cdot \cos \psi$  as photospheric boundary conditions at  $z = z_0$ , where  $B_{\parallel}$  is the observed  $V/I$  value, binned for computer memory reasons, and  $\psi$  is the angle between the  $z$  axis and the radial direction at the solar disk center, taking into account projection effects.

The extrapolations were performed for the SST magnetograms obtained at 8:58 UT and 9:30 UT, and the *Hinode*/SOT magnetograms taken at 8:10, 8:42 and 8:57 UT. The geometry and topology of the extrapolated magnetic fields are not sensitive to the exact value of the conversion factor between  $V/I$  and the magnetic field, provided this factor is nearly constant throughout the observed FOV.

In the extrapolations, the deprojected magnetogram was inserted into a wider region of  $L^2 \text{ Mm}^2$  (using various  $L$  between 200 and 340 Mm) with zero vertical component  $B_z$ , so as to minimize the aliasing effects resulting from the periodic boundary conditions along the  $x$  and  $y$  axes. The total  $B_z$  at  $z = z_0$  was developed into Fourier eigenmodes, using a resolution of  $1024 \times 1024$ . Hence, the original resolution of the magnetogram was degraded by a factor  $\sim 5.1$ . This degradation does not change the overall topology and field line connections. Using the linear force-free field equation

$$\nabla \times \mathbf{B} = \alpha \mathbf{B}, \quad (3)$$

the  $B_{x,y}$  components at  $z = z_0$ , as well as all three components of  $\mathbf{B}$  at various  $z > z_0$ , were calculated according to the value of the force-free parameter  $\alpha$ . In our study,  $\alpha$  was a free parameter with (maximum and minimum) resonant values  $\alpha' = \pm 2\pi/2L$ . The potential fields were calculated using  $\alpha = 0$ . The output vector  $\mathbf{B}$  was then

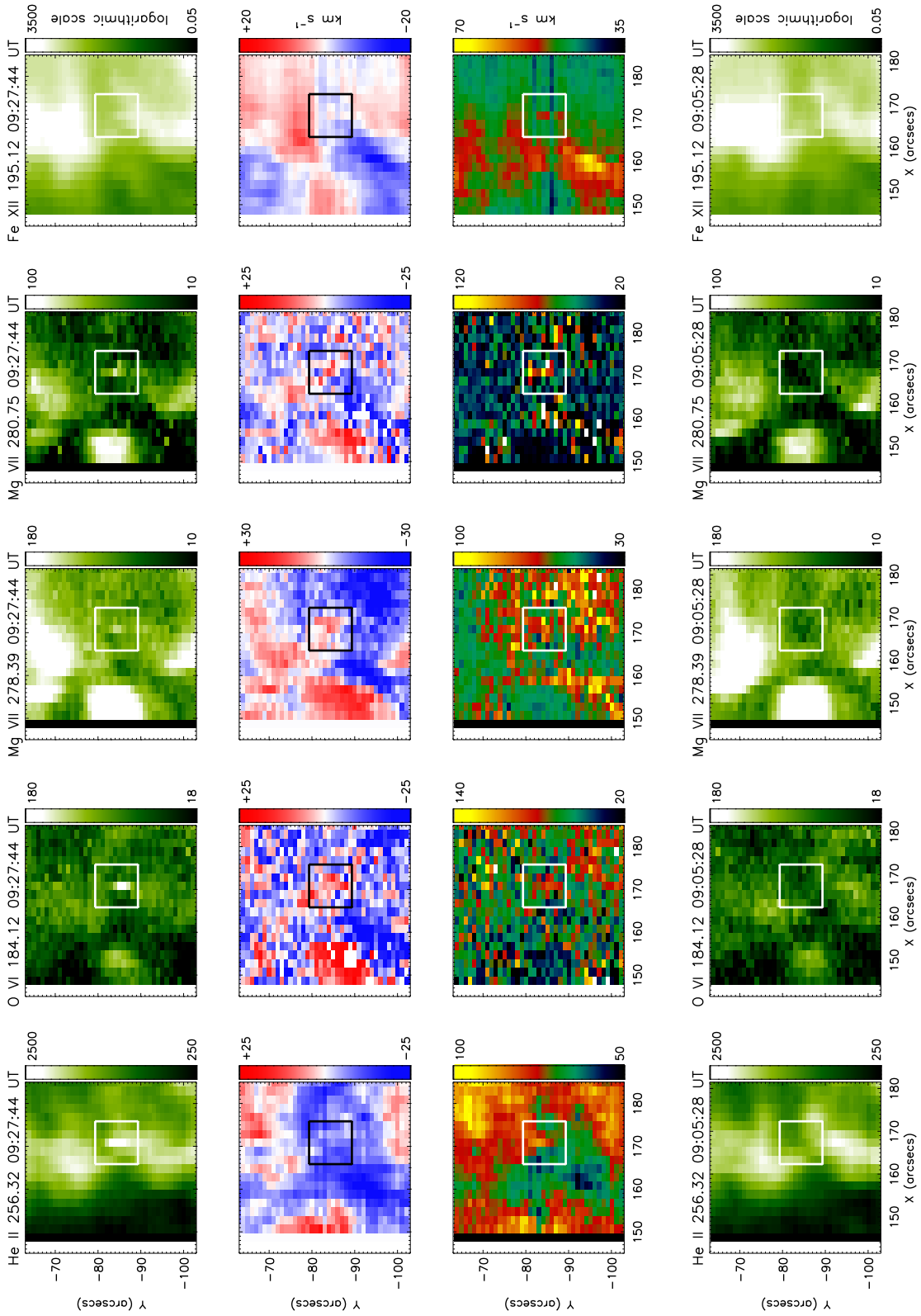


**Figure 11.** Maps of radiance (*first row*), Doppler velocity (*second row*), and line width (*third row*) obtained for five EUV lines observed by EIS during the scan started at 9:27 UT. The squares indicate the region where the brightenings have been observed. For comparison, we also report the radiance map (*fourth row*) for the same five lines during the previous scan, started at 9:05 UT.

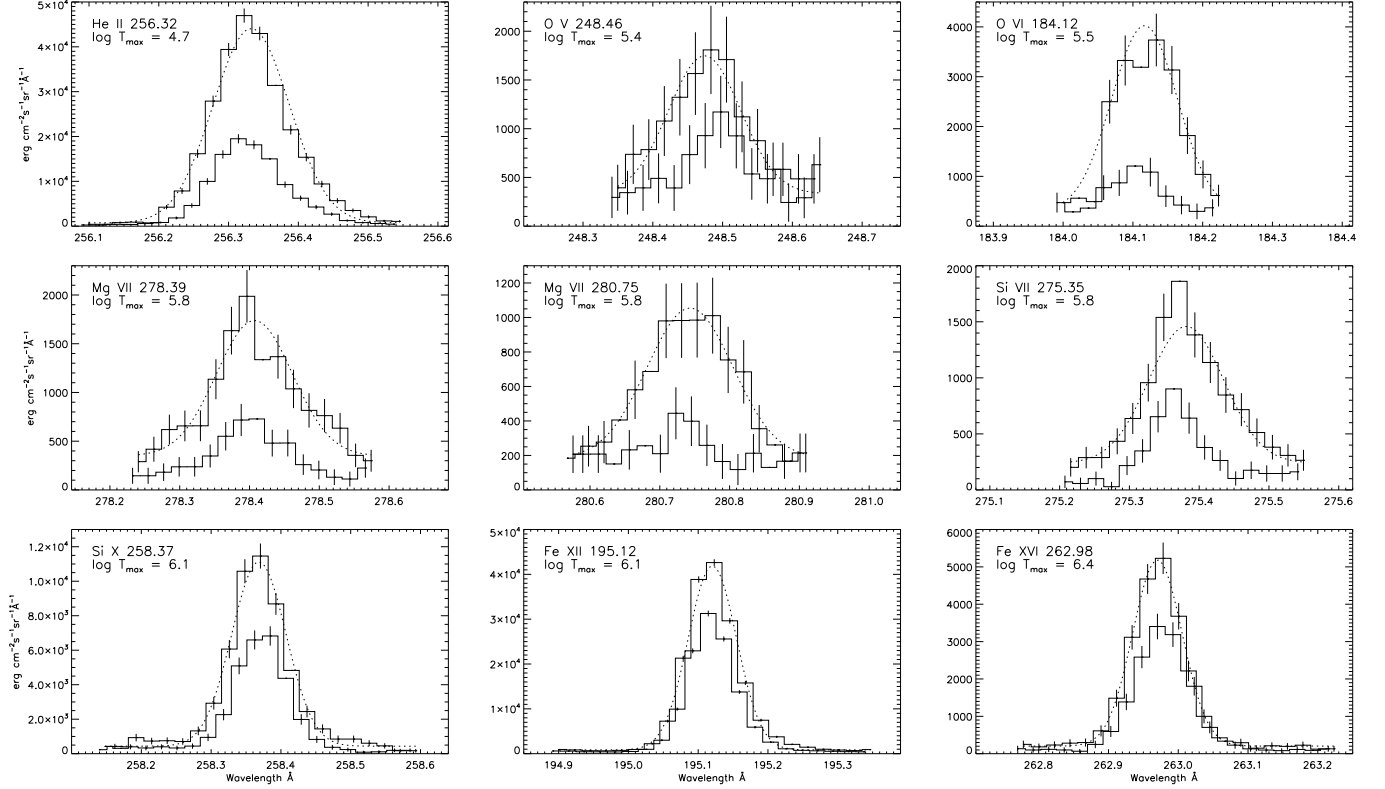


**Figure 12.** Intensity profiles of nine EUV lines with increasing ion temperatures, observed by EIS before (*solid line*) and during the brightenings (*solid thick line*). Dotted lines represent Gaussian fits to the profiles at 9:45 UT.

**Table 1**  
EUV parameters

Ion	$\lambda_0$ (Å)	$T_{\max}$ (K)	$I_b$	$v_D$ (km s $^{-1}$ )	FWHM (Å)	$v_{\text{non-th}}$ (km s $^{-1}$ )	$v_{\text{th}}$ (km s $^{-1}$ )
He II	256.32	$10^{4.7}$	2.9	$-7 \pm 1$	$0.135 \pm 0.002$	$85 \pm 2$	14.4
O V	248.46	$10^{5.4}$	5.1	$5 \pm 10$	$0.13 \pm 0.04$	$87 \pm 30$	15.6
O VI	184.12	$10^{5.5}$	4.9	$5 \pm 8$	$0.11 \pm 0.02$	$86 \pm 30$	17.7
Mg VII	278.39	$10^{5.8}$	3.6	$12 \pm 5$	$0.12 \pm 0.02$	$75 \pm 10$	20.8
Mg VII	280.75	$10^{5.8}$	9.7	$16 \pm 10$	$0.18 \pm 0.05$	$110 \pm 30$	20.8
Si VII	275.35	$10^{5.8}$	3.4	$20 \pm 5$	$0.15 \pm 0.02$	$90 \pm 10$	18.5
Si X	258.37	$10^{6.1}$	1.6	$-3 \pm 2$	$0.084 \pm 0.004$	$34 \pm 5$	28.6
Fe XII	195.12	$10^{6.1}$	1.4	$1.0 \pm 0.6$	$0.083 \pm 0.001$	$52 \pm 1$	20.0
Fe XVI	262.98	$10^{6.4}$	1.4	$-8 \pm 2$	$0.083 \pm 0.004$	$32 \pm 5$	28.0

**Note.** — Rest wavelength  $\lambda_0$  from the CHIANTI database, ion temperature  $T_{\max}$ , ratio between the integrated intensity during and before the brightening  $I_b$ , Doppler velocity  $v_D$ , line width at half maximum FWHM, non-thermal velocity  $v_{\text{non-th}}$ , and (tabulated) thermal velocity  $v_{\text{th}}$  in the pixel where the brightening occurs, for a sample of EUV lines observed by EIS.

written in a  $301 \times 301$  mesh, with the smallest cell being  $D = 0.17$  Mm around the EFR, and slowly increasing toward the edges of the box in the  $x$  and  $y$  directions. For  $z > 0$ ,  $\mathbf{B}$  was calculated in 201 layers above the plane of the magnetogram, the smallest interval in  $z$  being 0.13 Mm, and slowly increasing up to  $z = z_0 + 100$  Mm.

#### 4.1. Fan-spine topology

We performed extrapolations of the five magnetograms listed above, for several values  $|\alpha| \leq 3/4 \alpha'$ . While the orientation of the field lines connecting the main polarities of the active region is sensitive to  $\alpha$ -variations, the global topology of the magnetic field as well as the overall orientation of the field lines above the EFR change very little from one extrapolation to the next. So, for simplicity, we hereafter focus on the results of the potential field extrapolation of the SST magnetogram taken at 9:30 UT (shown in Figs. 13 and 14).

An asymmetric null point is observed above the EFR. The strength of the large-scale magnetic field of the active region makes this null to be located on the west side of the main positive polarity of the EFR, slightly NW from the location of the Ca II H and H $\alpha$  brightenings. Depending on the extrapolation, the altitude of the 3D null point is typically 150 – 400 km above that of the magnetogram. Since the formation height of the Fe I 630.25 nm line is  $z_0 \simeq 250$  km above  $\tau = 1$ , the null point is located just above the temperature minimum ( $z \geq 400$  km), right at the base of the chromosphere.

The magnetic field connectivity around the null point may be regarded as being a typical quadrupolar configuration in 2D, here an EW oriented  $-; +; -, +$ , where the first  $+$  polarity is the positive flux concentration of the EFR, and the second  $+$  is the extended western positive polarity of the active region. The magnetic configuration, however, is fully 3D. Understanding the sequence of reconnection events that may have led to the observed activity requires a 3D analysis.

As for all 3D null points, a fan surface and a singular spine field line originate from the null. On the one hand, the fan surface forms a dome which encloses the positive polarity of the EFR (surrounded by a closed polarity inversion line as shown in Fig. 13a). On the other hand, the spine connects the EFR to the distant western positive polarity of the active region. For relatively low  $\alpha$  values, the spine field line (which corresponds to the first eigenvector of the null point) is EW oriented and almost parallel to the H $\alpha$  surges (compare the dark blue line in Fig. 13a and the surge in Fig. 3).

The null point is a so-called “improper null” (i.e., it is non-axisymmetric around the spine axis, due to the different values of its two fan-related eigenvalues). In all the extrapolations, the eigenvalue of the eigenvector oriented in the NS direction is several times smaller than that one oriented in EW direction, so that magnetic field lines just above or below the fan surface are predominantly EW oriented. This static configuration is similar to that described by Masson et al. (2009). The structure of the fan is very robust to changing the lower boundary conditions (the magnetogram) or the force-free parameter  $\alpha$  for a given magnetogram. The former is a natural consequence of the strength of the overlying EW oriented bipolar field, which does not change significantly with time; the latter is due to the well-known insensitivity of

small-scale loops to  $\alpha$ -variations in the linear force-free field approximation (Alissandrakis 1981).

#### 4.2. Interpretation of the H $\alpha$ surges and Ca II H brightenings

To understand the origin of the observed surges and chromospheric brightenings, one first needs to know whether the null point topology found in the extrapolations existed prior to the event (as, e.g., in the jet model by Pariat et al. 2010) or if it was dynamically formed while the surges were launched (as, e.g., in the so-called two-step reconnection model by Török et al. 2009 or in the emergence-driven jet model by Moreno-Insertis et al. 2008). The SST magnetograms clearly show that a positive flux concentration was present in the dispersed negative polarity of the active region several tens of minutes before the appearance of the first surge (see Fig. 5 at 8:58 UT). The same feature can be observed since at least 7:50 UT in the magnetograms taken by *Hinode* (Guglielmino et al. 2008). The early existence of this parasitic polarity and the finding of a null point above it in all the extrapolations imply that the surges were triggered in a pre-existing null point topology.

The SST magnetograms shows the emergence of a new small bipole at about 9:18 UT, right before the first surge. It appears at the NE of the main positive polarity of the EFR. Until 9:25 UT, the bipole has an elongated shape with curly flux concentrations that look like those found in various MHD simulations of the emergence of sub-photospheric twisted flux ropes. This indicates the local presence of magnetic shear, and maybe twist, above the photosphere. Because of the shear/twist, the potential and LFFF extrapolations fail to connect the two polarities of the elongated structure. However, since the bipole is oriented in the NE-SW direction, we know that the emerging field lines make an angle of several tens of degrees with the overlaying field lines (see the green and cyan fan field lines of the null point in Fig. 13a).

Fig. 13b shows an EW oriented red field line that overlays the EFR and is located beneath the fan surface of the null point. Shortly after the beginning of the emergence of the twisted bipole, the lowermost growing sheared field lines could have pushed upwards this pre-existing fan-related red arcade. As a consequence, the red arcade would have reconnected with the long pink field lines located westward of it, forming new connections: one long field line (green in Fig. 13b) and one short arcade (yellow in Fig. 13b). In this scenario, H $\alpha$  surges would occur along the green field line (which is close to, but slightly south from, the spine of the null point), and bright Ca II H flare-like loops would form at the position of the yellow field lines (which are south from the pre-existing positive flux concentration). This is exactly what is seen in the observations.

The scenario described above may also explain why several surges are observed, and why the Ca II H emission gradually increases with time. Indeed, as more and more sheared/twisted field lines emerge, all the overlying, nearly-potential arcades would reconnect, leaving room for the sheared field lines themselves to undergo reconnection processes. Also, since the time sequence of magnetograms suggests the rise of a sub-photospheric twisted flux rope, the emerging field lines must be more and more sheared with time. This means that also the reconnection

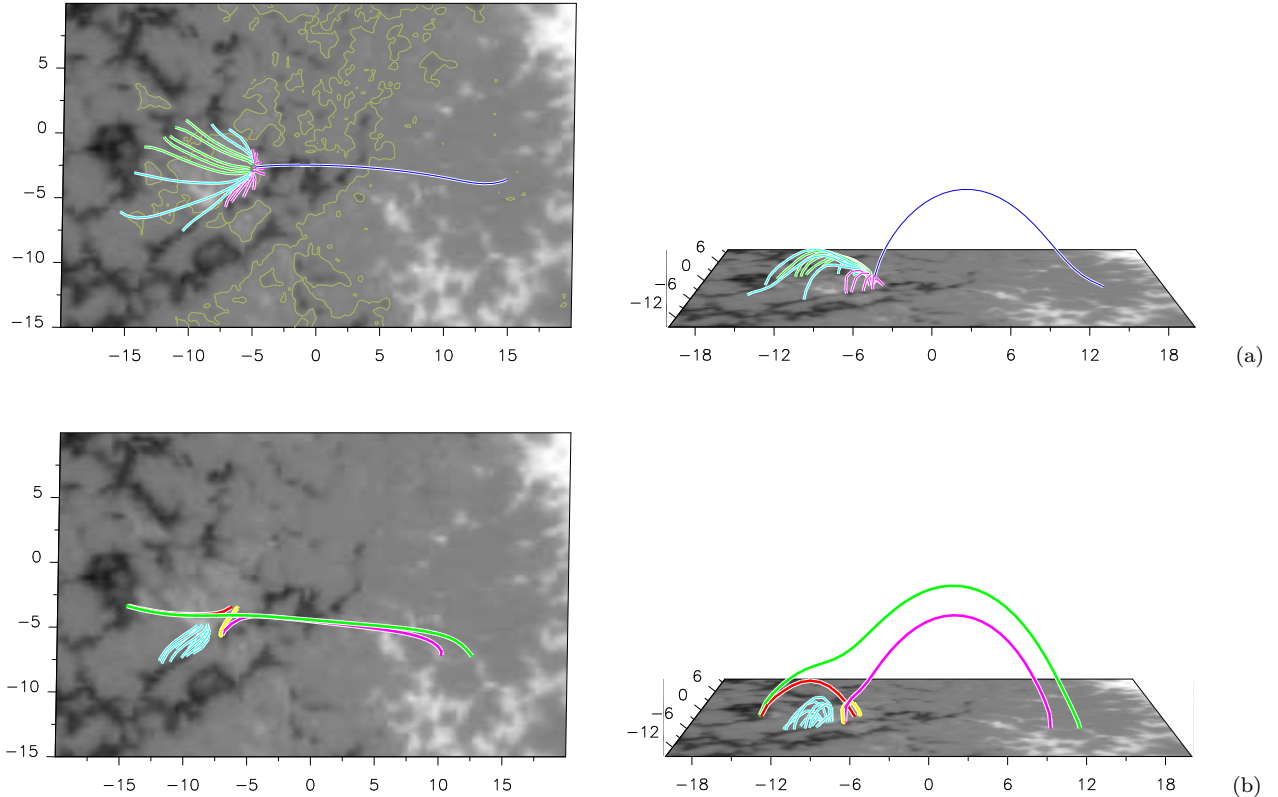


**Figure 13.** Magnetic field configuration of the active region around the EFR. The left column shows projections as viewed from Earth. The right column shows lateral perspectives looking toward solar north, with the  $z$  axis stretched by a factor two for better visibility of magnetic field lines. *Top:* Separatrix field lines emanating from the null point in the potential field extrapolation of the SST magnetogram acquired at 9:30 UT. The dark blue line is the spine field line, and other colored lines are fan field lines. The background image represents  $B_z$  at  $z = z_0$ , and yellow contours indicate polarity inversion lines. *Bottom:* Four selected field lines crossing each other slightly south from the null point, with neighboring NW-SE low altitude field lines (cyan). The cyan/red/yellow field lines are enclosed by the fan surface.

must involve field lines that are more and more sheared. As a consequence, non-smooth vertical shear profiles in the emerging/reconnecting field lines should naturally lead to non-smooth reconnection sequences, therefore to distinct surges. In addition, the reconnections should become more energetic with time since they involve field lines that contain more and more free magnetic energy, thus leading to brighter emissions in the Ca II H line core.

One may argue that this set of (red; pink, green; yellow) field lines cannot reconnect – and thus that our interpretation is invalid – because it is not exactly located at the null point. Two counter-arguments can be given. First, the exact position of the null point is not known, as it is sensitive to variations of the  $\alpha$  parameter. If the field were non-potential, the null point could have been located right on the side of the red arcade. Second, it has been shown by Masson et al. (2009) that, under some conditions, a (red) field line initially anchored several Mm away from a null point can still reconnect at it, and that the (green) reconnected field line can eventually reach a position away from the spine of the null, as these lines can “slip-run” towards and away from it. The condition found by Masson et al. (2009) for this to happen is the existence of an elongated quasi-separatrix layer in which the spine is embedded, which is associated with the asymmetric property of the null point. As the null point is “improper” in all the extrapolations, the condi-

tion for the occurrence of coupled slip-running/null-point reconnection is satisfied.

## 5. SUMMARY

In this paper we have studied the configuration and evolution of a small-scale EFR using very high-resolution filtergrams taken at the SST. We have also analyzed simultaneous observations performed by the three telescopes aboard *Hinode*. The measurements cover a period of  $\sim 2$  hours and a broad wavelength range from the visible to soft X-rays.

These data have allowed us to observe the flux emergence event in its entirety, and to study the characteristics of the EFR and its temporal evolution at different heights in the solar atmosphere.

The photospheric evolution of the emerging flux in the G band is characterized by the distortion of the granulation pattern and the appearance of transient dark lanes. The dark lanes are associated with horizontal fields and upflows (Guglielmino et al. 2008). This confirms recent high-resolution observations and numerical simulations. Moreover, the sequence of Fe I magnetograms shows that the field does not emerge as a monolithic bipole, but as a series of small-scale, mixed-polarity flux patches.

Various phenomena indicating the release of energy and consequent plasma heating, as well as the formation of jets, occurred at the EFR site: brightenings in Ca II H, H $\alpha$ , and EUV lines, intensity enhancements in

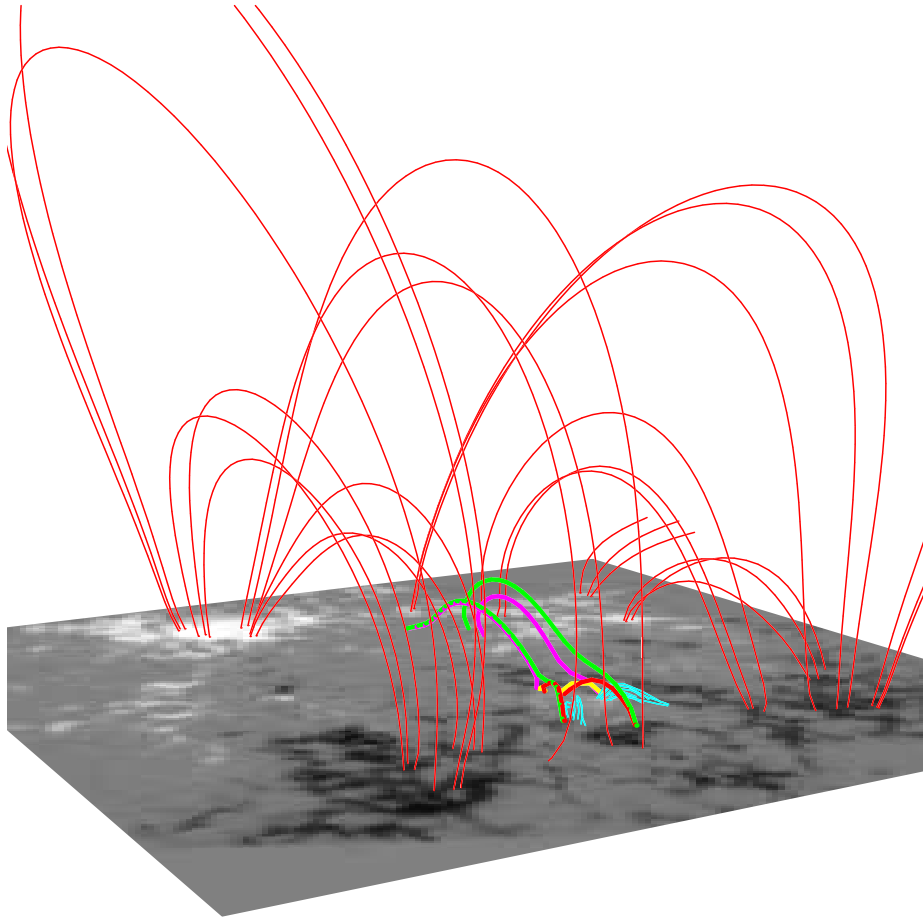


**Figure 14.** Large-scale view of the potential extrapolation shown in Fig. 13. Thin red lines represent the field lines connecting the main polarities of the active region. Thick colored lines show the same groups of field lines displayed in Fig. 13b. The path of the long thick red and green lines closely follows that of the spine of the null point.

X-rays, and  $H\alpha$  surges. We have analyzed the spatial and temporal relationship between all these features, in order to clarify the evolution of the underlying process.

The brightness enhancements were first seen in the chromospheric Ca II H line, which has the lowest formation height. The beginning of the Ca II H enhancement occurred at the time the flux started to increase in the upper photosphere, around 9:10 UT. An  $H\alpha$  surge was observed at 9:23 UT, and the Ca II H intensity continued to grow until a localized, intense brightening appeared at 9:27 UT. The  $H\alpha$  intensity began to rise at 9:27 UT, producing a well-defined brightening at 9:39 UT, so there was a temporal delay of more than 10 minutes with respect to Ca II H. This is consistent with the higher formation height of the  $H\alpha$  measurements. However, the  $H\alpha$  and Ca II H brightness peaked almost simultaneously, around 9:45 UT. This was also the time of the maximum X-ray intensity detected with *Hinode* at the position of the EFR. Two more  $H\alpha$  surges appeared during the emergence event, at around 9:37 and 9:52 UT. The observed time lags support the interpretation of all these phenomena as being caused by magnetic reconnection at low altitude in the atmosphere.

The EIS measurements show localized brightenings in the coldest EUV lines, with small flows that are not significant or extend over much larger areas. The brightness enhancement decreases with increasing ion temperature (i.e., formation height) of the lines. Moreover, we detect

strong non-thermal broadenings except in the hot Fe XII 195 Å line.

We have investigated the relationship between the evolution of the flux and the onset of jet-like activity. Yoshimura et al. (2003) found that surges appear during the declining phase of the magnetic flux, due to cancellation between the emerging flux and the pre-existing fields of opposite polarity. On the contrary, in our observations the surges set up while the flux was still increasing in the upper photosphere (see Fig. 4). This suggests that the magnetic reconnections that supplied the energy of the surges occurred above the formation height of the Na I D1 magnetograms, probably in the low chromosphere.

All these findings point to the emergence event as the likely trigger of the reconnection process, due to the interactions between two flux systems: the pre-existing arcades and the EFR field lines. In order to shed light on this issue, we have performed LFFF extrapolations to determine the coronal connectivity above the EFR and the possible reconfiguration of the ambient and emerging field lines.

The scenario suggested by the extrapolations is the following: as the positive polarity of the EFR appears on the surface with its conjugate negative polarity, the foot-point separation increases due to the diverging motion, so the emerging lines bulge upwards. They therefore push the overlying arcades, which can reconnect to produce

a set of long loops (reminiscent of the  $H\alpha$  surges) and smaller loops (reminiscent of the observed small brightening regions). A fan-spine topology forms, and its structure is very stable against changes in the extrapolation parameters, like the  $\alpha$ -value or the boundary conditions.

The 3D null point lies quite low in the atmosphere, 150 – 400 km above the formation height of the Fe I 630.25 nm line. Thus, it is located at the base of the chromosphere ( $\sim 500$  km). The observed  $H\alpha$  surges are nearly cospatial with field lines produced by the reconnection of arcades overlying the EFR and other active region loops. Therefore, they could represent reconnection jets formed by accelerated material propagating along those lines. The emerging field lines would not participate directly in the surges, but would indirectly trigger them by pressing the ambient fields together and forcing their reconnection.

Török et al. (2009) modeled the emergence of a twisted flux tube into a potential field arcade, showing that a 3D null point topology is produced in the corona. This configuration results from a two-step reconnection process, which transfers the stress of the emerging magnetic lines (twist or shear) into the coronal arcades by means of a torsional Alfvén wave, with the onset of a jet. In our case, it seems that the null point had already formed when the SST started to observe – most probably as a result of the emergence of the very first positive flux patches –, so the situation is closer to that modeled by, e.g., Pariat et al. (2010). We thus favor the simple explanation given above as opposed to a more complex two-step reconnection process, although the former cannot be ruled out completely.

Our analysis combines multi-wavelength observations and detailed magnetic field extrapolations. This has enabled us to understand the complex sequence of events associated with the EFR as being the result of magnetic reconnection triggered by the emergence of new flux into the atmosphere. Processes like the one considered here are difficult to interpret without the help of high resolution measurements and extrapolations. Both techniques have reached a sufficient degree of maturity, so we believe that this kind of analyses will become standard practice in the near future.

It is a pleasure to thank V. Domingo for his help with the SST observations, J.A. Bonet for advice concerning the MOMFBD technique, I. Pagano for useful suggestions in the UV analysis, and all the scientists of the *Hinode* team for the operation of the instruments. This work was started while one of us (S. Guglielmino) was a Visiting Scientist at the Instituto de Astrofísica de Andalucía. Financial support by the European Commission through the SOLAIRE Network (MTRN-CT-2006-035484) is gratefully acknowledged. This research has been partly funded by the Spanish Ministerio de Ciencia e Innovación through projects ESP2006-13030-C06-02, PCI2006-A7-0624, and Programa de Acceso a Infraestructuras Científicas. The Swedish 1-m Solar Telescope is operated by the Institute for Solar Physics of the Royal Swedish Academy of Sciences in the Spanish Observatorio del Roque de los Muchachos of the Instituto de Astrofísica de Canarias. *Hinode* is a Japanese mission developed and launched by ISAS/JAXA, with NAOJ as domestic partner and NASA and STFC (UK

as international partners. It is operated by these agencies in co-operation with ESA and NSC (Norway). Use of NASA's Astrophysical Data System is gratefully acknowledged.

*Facilities:* SST, Hinode.

## REFERENCES

- Alissandrakis, C.E. 1981, *A&A*, 100, 197  
 Archontis, V., Moreno-Insertis, F., Galsgaard, K., Hood, A., & O'Shea, E. 2004, *A&A*, 426, 1047  
 Archontis, V., Moreno-Insertis, F., Galsgaard, K., & Hood, A. W. 2005, *ApJ*, 635, 1299  
 Brooks, D. H., Kurokawa, H., & Berger, T. E. 2007, *ApJ*, 656, 1197  
 Brown, C. M., Feldman, U., Seely, J. F., Korendyke, C. M., & Hara, H. 2008, *ApJS*, 176, 511  
 Cabrera Solana, D., Bellot Rubio, L. R., & del Toro Iniesta, J. C. 2005, *A&A*, 439, 687  
 Canfield, R. C., Reardon, K. P., Leka, K. D., Shibata, K., Yokoyama, T., & Shimojo, M. 1996, *ApJ*, 464, 1016  
 Chae, J., Qiu, J., Wang, H., & Goode, P. R. 1999, *ApJ*, 513, L75  
 Cheung, M. C. M., Schüssler, M., & Moreno-Insertis, F. 2007, *A&A*, 467, 703  
 Cheung, M. C. M., Schüssler, M., Tarbell, T. D., & Title, A. M. 2008, *ApJ*, 687, 1373  
 Culhane, J. L., et al. 2007, *Sol. Phys.*, 243, 19  
 Dere, K. P., Landi, E., Mason, H. E., Monsignori Fossi, B. C., & Young, P. R. 1997, *A&AS*, 125, 149  
 Ellerman, F. 1917, *ApJ*, 46, 298  
 Fan, Y. 2009, *Living Rev. Solar Phys.*, 6, 4 (URL: <http://www.livingreviews.org/lrsp-2009-4>)  
 Galsgaard, K., Archontis, V., Moreno-Insertis, F., & Hood, A. W. 2007, *ApJ*, 666, 516  
 Georgoulis, M. K., Rust, D. M., Bernasconi, P. N., & Schmieder, B. 2002, *ApJ*, 575, 506  
 Golub, L., et al. 2007, *Sol. Phys.*, 243, 63  
 Guglielmino, S. L., Zuccarello, F., Romano, P., & Bellot Rubio, L. R. 2008, *ApJ*, 688, L111  
 Harra, L. K., Williams, D. R., Wallace, A. J., Magara, T., Hara, H., Tsuneta, S., Sterling, A. C., & Doschek, G. A. 2009, *ApJ*, 691, L99  
 Heggland, L., DePontieu, B., & Hansteen, V. H. 2009, *ApJ*, 702, 1  
 Ishikawa, R., et al. 2007, *A&A*, 472, 911  
 Isobe, H., Miyagoshi, T., Shibata, K., & Yokoyama, T. 2005, *Nature*, 434, 478  
 Kosugi, T., et al. 2007, *Sol. Phys.*, 243, 3  
 Kurokawa, H., & Kawai, G. 1993, *IAU Colloq. 141: The Magnetic and Velocity Fields of Solar Active Regions*, 46, 507  
 Landi, E., Del Zanna, G., Young, P. R., Dere, K. P., Mason, H. E., & Landini, M. 2006, *ApJS*, 162, 261  
 Liu, Y., & Kurokawa, H. 2004, *ApJ*, 610, 1136  
 Mariska, J. T., Warren, H. P., Ugarte-Urra, I., Brooks, D. H., Williams, D. R., & Hara, H. 2007, *PASJ*, 59, 713  
 Martínez-Sykora, J., Hansteen, V., & Carlsson, M. 2008, *ApJ*, 679, 871  
 Martínez-Sykora, J., Hansteen, V., DePontieu, B., & Carlsson, M. 2009, *ApJ*, 701, 1569  
 Masson, S., Pariat, E., Aulanier, G., & Schrijver, C. J. 2009, *ApJ*, 700, 559  
 Matsumoto, T., et al. 2008, *PASJ*, 60, 95  
 Moreno-Insertis, F., Galsgaard, K., & Ugarte-Urra, I. 2008, *ApJ*, 673, L211  
 November, L. J., & Simon, G. W. 1988, *ApJ*, 333, 427  
 Otsuji, K., et al. 2007, *PASJ*, 59, 649  
 Pariat, E., Antiochos, S. K., & DeVore, C. R. 2010, *ApJ*, 714, 1762  
 Phillips, K. J. H., Feldman, U. & Landi, E. 2008, *Ultraviolet and X-ray Spectroscopy of the Solar Atmosphere* Cambridge : Cambridge University Press.  
 Scharmer, G. B., Bjelksjo, K., Korhonen, T. K., Lindberg, B., & Petterson, B. 2003, *Proc. SPIE*, 4853, 341  
 Shibata, K., et al. 1992, *PASJ*, 44, L173  
 Shimizu, T., et al. 2007, *PASJ*, 59, 845

- Stix, M. 2002, *The Sun: an introduction* – 2nd ed. Berlin : Springer.
- Strous, L. H., & Zwaan, C. 1999, *ApJ*, 527, 435
- Title, A. M., & Rosenberg, W. J. 1981, *Opt. Eng.*, 20, 815
- Török, T., Aulanier, G., Schmieder, B., Reeves, K. K., & Golub, L. 2009, *ApJ*, 704, 485
- Tortosa-Andreu, A., & Moreno-Insertis, F. 2009, *A&A*, 507, 949
- Tsuneta, S., et al. 2008, *Sol. Phys.*, 249, 167
- van Noort, M., Rouppe van der Voort, L., Löfdahl, M. G. 2005, *Sol. Phys.*, 228, 191
- van Noort, M. J., & Rouppe van der Voort, L. H. M. 2008, *A&A*, 489, 429
- Vernazza, J. E., Avrett, E. H., & Loeser, R. 1981, *ApJS*, 45, 635
- Wallace, A., et al. 2010, *Sol. Phys.*, submitted
- Yokoyama, T., & Shibata, K. 1995, *Nature*, 375, 42
- Yokoyama, T., & Shibata, K. 1996, *PASJ*, 48, 353
- Yoshimura, K., Kurokawa, H., Shimojo, M., & Shine, R. 2003, *PASJ*, 55, 313
- Young, P. R., Watanabe, T., Hara, H., & Mariska, J. T. 2009, *A&A*, 495, 58
- Young, P. R., et al. 2007, *PASJ*, 59, 727
- Young, P. R., et al. 2007, *PASJ*, 59, 857
- Zhang, J., Wang, J., & Liu, Y. 2000, *A&A*, 361, 759
- Zuccarello, F., Guglielmino, S. L., Battiato, V., Contarino, L., Spadaro, D., & Romano, P. 2009, *Acta Geophysica*, 57, 15